Research Article

Discrete Model Reference Adaptive Control for Gimbal Servosystem of Control Moment Gyro with Harmonic Drive

Bangcheng Han,[1,2] Yanpeng Chen,[1,2] Haitao Li,[1,2] and Lianhui Yang[1,2]

[1] Science and Technology on Inertial Laboratory, Beihang University, Beijing 100191, China
[2] Fundamental Science on Novel Inertial Instrument & Navigation System Technology Laboratory,
  Beihang University, Beijing 100191, China

Correspondence should be addressed to Yanpeng Chen; chenyanpeng87@163.com

The double-gimbal control moment gyro (DGCMG) demands that the gimbal servosystem should have fast response and small overshoot. But due to the low and nonlinear torsional stiffness of harmonic drive, the gimbal servo-system has poor dynamic performance with large overshoot and low bandwidth. In order to improve the dynamic performance of gimbal servo-system, a model reference adaptive control (MRAC) law is introduced in this paper. The model of DGCMG gimbal servo-system with harmonic drive is established, and the adaptive control law based on POPOV super stable theory is designed. The MATLAB simulation results are provided to verify the effectiveness of the proposed control algorithm. The experimental results indicate that the MRAC could increase the bandwidth of gimbal servo-system to 3 Hz and improve the dynamic performance with small overshoot.

1. Introduction

With the superior characteristics of large torque amplification and high precision, the control moment gyros (CMGs) are the key actuators for the attitude control system of space stations, satellites, and other crafts [1, 2]. CMG mainly consists of gimbal servosystem and high-speed rotor system. According to the number of the gimbal DOF (degree of freedom), the CMG can be divided into single-gimbal CMG (SGCMG) and double-gimbal CMG (DGCMG) [3, 4]. Depending on the supporting manner of high-speed rotor, CMG can be divided into mechanical bearing CMG and magnetically suspended CMG [5, 6].

The CMG outputs gyro moment through changing the direction of high-speed rotor angular momentum by driving the gimbal. The gyro moment equation is

$$\vec{M} = \vec{H} \times \vec{\omega}, \tag{1}$$

where $\vec{M}$ is gyro moment, $\vec{\omega}$ is gimbal angular velocity, and $\vec{H}$ is high-speed rotor angular momentum. As shown in Figure 1, the angular velocity of inner and outer gimbal is,

respectively, ω_x and ω_y. $\vec{H}$ is the high-speed rotor angular momentum. $\vec{M}_x$ and $\vec{M}_y$ are gyro moments

$$\vec{M}_x = \vec{H} \times \vec{\omega}_x, \qquad \vec{M}_y = \vec{H} \times \vec{\omega}_y. \tag{2}$$

$\vec{M}_x$ and $\vec{M}_y$ should be overcome by the torque motor of gimbal servosystem. Considering space applications, there are strict requirements for the size and weight of CMG. In order to reduce the weight and volume of torque motor, the DGCMG gimbal servosystem in this paper employs harmonic drive as shown in Figure 2.

Compared to other speed reducers, harmonic drives have many useful properties including near-zero backlash, high gear ratio, light weight, and compact size. They have high velocity reduction in a relatively small package permitting and high torque amplification with only small motors. Hence they are widely used in precision application including industrial and space robots, medical equipment, measuring instruments, and military defense equipment [7].

Because of the structure characteristics and assembly error, harmonic drives also have some nonlinear characters like nonlinear torsion-stiffness, nonlinear friction, kinematic
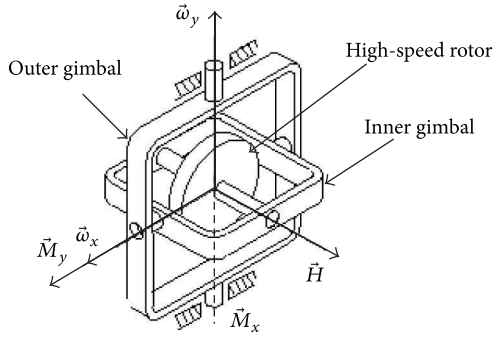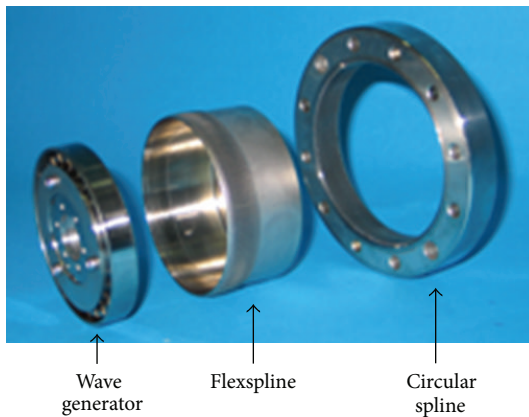
FIGURE 1: Structure diagram of DGCMG.

FIGURE 2: Harmonic drive.

FIGURE 3: View of DGCMG.

error, and so forth, which degrade system transmission performance [8, 9]. Particularly, due to the thin-wall structure of flexspline, harmonic drives have a low and nonlinear torsion-stiffness [10]. The DGCMG gimbal servosystem is actually a two-mass system with flexible joint [11, 12]. The joint flexibility could bring poor dynamic performance. In [12], an analysis of control structure for electrical drive system with elastic joint is carried out. To solve this problem, many literatures have been reported. In [13], a PI controller with an analytic gain selection is proposed. The gains are given as functions of system parameters and desired dominant closed-loop poles. Due to the nonlinearity, the PI controller with fixed proportional and integral coefficients could not always meet the requirements. Several adaptive control schemes with torque feedback are introduced in [14–16]. In [15], the adaptive control algorithm based on virtual decomposition could improve the tracking performance obviously compared to PID controller. Other control laws have been proposed for flexible joint. In [17], a model following adaptive control method for nonlinear flexible joint robots with time-varying parameters is introduced. An LQGR/LQG control for trajectory tracking control of flexible joint robotic system is presented in [18]. In [19], an H^∞ controller has a good step-response with the exception of larger overshot than PID controller.

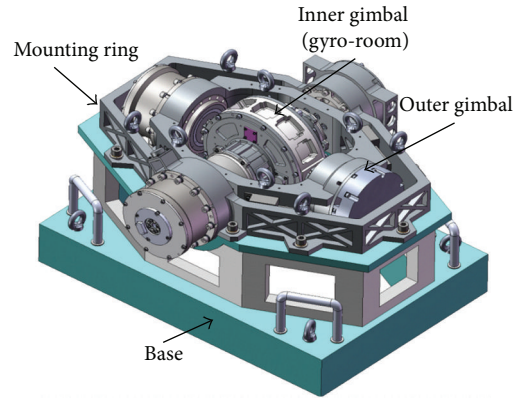The model reference adaptive control (MRAC) is a traditional adaptive control method which has been widely

adopted in engineering practice, such as synchronization motor control [20, 21], power devices [22, 23]. Compared to conventional controllers, MRAC could achieve high precision performance under the condition of friction, load disturbance, parameter variation, and other nonlinear factors. In [20], an MRAC-based current control scheme of PMSM is presented to improve steady-state response degraded under the motor parameter variation. In [21], MRAC is designed for PMSM servosystem. The results indicate that MRAC has the features of smaller current fluctuation and faster regulated speed than the systems using PI controller.

In this paper, a model reference adaptive control strategy is introduced to improve the dynamic performance of DGCMG gimbal servosystem with harmonic drive. Because only the input, output, and error are used and the measurement of the torque is not required, the proposed method is simple. The reference model for MRAC is selected according to the requirement for dynamic performance with fast response and small overshoot. The discrete POPOV super stable theory is used to design the adaptive controller. Last the performance of MRAC is compared with that of a conventional PID controller.

This paper is organized as follows: Section 2 outlines the model of gimbal servosystem with harmonic drive; the selection of reference model is presented in Section 3; in Section 4, the discrete adaptive controller is designed based on POPOV super stable theory; in Section 5, the simulation analyses are presented; the experimental results in DGCMG are presented in Section 6.

2. The Model of Gimbal Servosystem with Harmonic Drive

As shown in Figures 1 and 3, DGCMG consists of inner and outer gimbal servosystems and a high-speed rotor system supported by inner gimbal (gyro-room). The mounting ring is fixed on a rigid base which is immobile in experiment.

The inner and outer gimbal servosystems have the similar framework with same torque motor and harmonic drive. What is different is the rotational inertia of load. They also
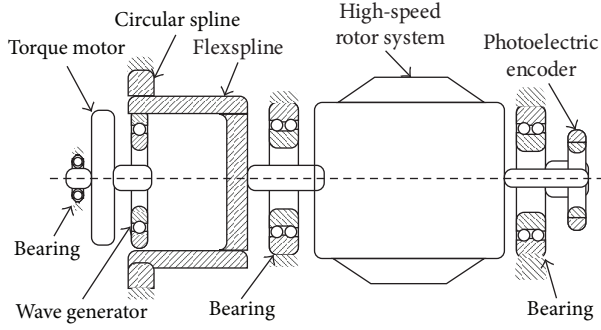
FIGURE 4: Structure diagram of inner gimbal.

apply the same control method and could be controlled independently. So only the inner gimbal is studied as an example in this paper. The outer gimbal could adopt the same control method with different parameters. The structure diagram of the inner gimbal servosystem is shown in Figure 4. The two ends of the gimbal are, respectively, named as motor terminal and load terminal. The motor terminal mainly contains of torque motor and harmonic drive. The load terminal mainly consists of high-speed rotor, gyro-room, and photoelectric encoder. The harmonic drive consists of circular spline, flexspline, and wave generator.

The electrical model of torque motor can be described as [24]

$$Ri_m + \frac{Ldi_m}{dt} + C_e\dot{\theta}_m = U,$$
$$T_m = C_l i_m. \tag{3}$$

The gimbal servosystem with harmonic drive is essentially a two-mass system [11]. The dynamic model is given as

$$J_m\ddot{\theta}_m + B_m\dot{\theta}_m + \frac{K_e\theta}{N} = T_m,$$
$$J_l\ddot{\theta}_l + B_l\dot{\theta}_l + T_f = K_e\theta, \tag{4}$$
$$\theta = \frac{\theta_m}{N} - \theta_l.$$

The gimbal control system has two control loops, speed loop and current loop. According to (3)-(4), the control diagram of the inner gimbal servosystem is shown in Figure 5. In Figure 5, $G_v(s)$ is the speed loop controller.

3. Reference Model Selection

The schematic diagram of MRAC is shown in Figure 6. r is the input of reference model and controlled object. The controlled object output y_p is the actual response, and the reference output y_m is the expected response of system. Define generalized error $e = y_m - y_p$. The adaptive controller adapts the parameters of $H(s)$ and $G(s)$ based on generalized error e. At last, e reaches to 0. That is, controlled object output has kept up with reference model output. The design of model reference controller mainly contains reference

model selection and adaptive controller design. The design of adaptive controller will be introduced in Section 4. The reference model is selected according to the requirement for dynamic performance and the structure characteristics of controlled object.

3.1. Controlled Object Model. In order to keep the fast dynamic response of current loop, the current loop and controlled object are treated as the generalized controlled object (dashed line frame of Figure 5). Only the speed loop is replaced with adaptive controller. The transfer function of the generalized controlled object is

$$\frac{\dot{\theta}_l}{i_{\text{ref}}} = \frac{C_l K_e K_c K_u}{a_4 s^4 + a_3 s^3 + a_2 s^2 + a_1 s + a_0}, \tag{5}$$

where

$$K_1 = RB_m + K_c K_u K_b K_s B_m + C_e C_l,$$

$$K_2 = R + K_c K_u K_b K_s,$$

$$K_3 = LB_m + RJ_m + K_c K_u K_b K_s J_m,$$

$$a_0 = NK_e K_1 + \frac{1}{N} K_e B_l K_2,$$

$$a_1 = N(K_1 B_l + K_e K_3) + \frac{1}{N} K_e (J_l K_2 + B_l L), \tag{6}$$

$$a_2 = N(J_l K_1 + K_e J_m L + K_3 B_l) + \frac{1}{N} J_l K_e L,$$

$$a_3 = N(K_3 J_l + J_m L B_l),$$

$$a_4 = NJ_l J_m L.$$

From (5), the controlled object is a fourth-order system. According real system parameters, the fourth-order system can be reduced to third-order system. The process of reducing order is as follows.

Define the electromagnetic time constant of torque motor by

$$T_e = \frac{L}{R}. \tag{7}$$

Define the electromechanical time constant of torque motor by

$$T_m = \frac{RJ_m}{C_e C_l}. \tag{8}$$

According to Table 1, (7) and (8) could be calculated: $T_e = 0.0001$ s, $T_m = 0.02$ s. Due to $T_m \gg T_e$, the effect of T_e to torque motor can be ignored, that is, $L = 0$. Because that damping coefficient B_l is small and the gimbal angle velocity $\dot{\theta}_l$ is also small (less than 0.1745 rad/s), the friction damping torque $B_l\dot{\theta}_l$ has little influence on gimbal system. So B_l can be also ignored, that is, $B_l = 0$. Thence, (5) can be simplified as (9) which is a third-order system:

$$\frac{\dot{\theta}_l}{i_{\text{ref}}} = \frac{C_l K_e K_c K_u}{b_3 s^3 + b_2 s^2 + b_1 s + b_0}, \tag{9}$$
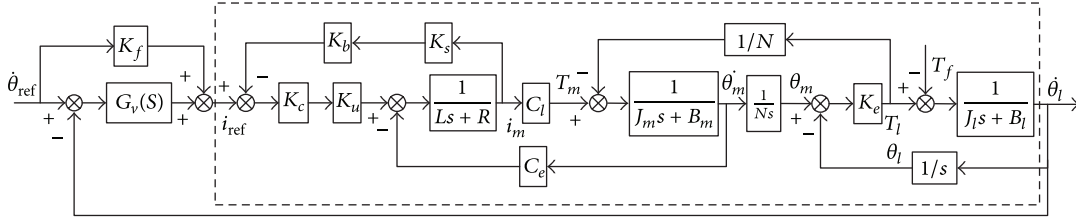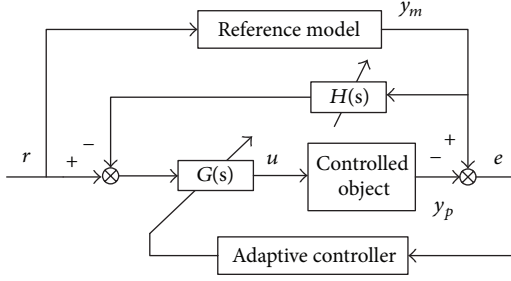
FIGURE 5: Control diagram of inner gimbal servosystem.

FIGURE 6: Schematic diagram of MRAC.

TABLE 1: System physical parameters.

Parameter	Value
L	1.2 mH
R	10.8 Ω
C_e	0.892 V/(rad/s)
C_l	0.774 N·m/A
K_s	789
K_u	0.056
J_m	0.0013 kg·m^2
J_l	0.0397 kg·m^2
B_m	0.043 N·m/(rad/s)
K_e	30000 N·m/rad
N	100

where

$$
\begin{aligned}
b_0 &= NK_e\left(RB_m + K_cK_uK_bK_sB_m + C_eC_l\right), \\
b_1 &= K_e\left(NJ_m + \frac{1}{N}J_l\right)\left(R + K_cK_uK_bK_s\right), \\
b_2 &= NJ_l\left(RB_m + K_cK_uK_bK_sB_m + C_eC_l\right), \\
b_3 &= NJ_mJ_l\left(R + K_cK_uK_bK_s\right).
\end{aligned}
\tag{10}
$$

In order to observe the physical significance of (9) and select the reference model easily, (9) is needed to be further described.

Define the mechanical resonance-frequency by

$$
\omega_n = \frac{1}{T} = \sqrt{\frac{K_e}{J_l}}.
\tag{11}
$$

Define the generalized electromechanical time constant by

$$
T_e = \frac{\left(R + K_cK_uK_bK_s\right)J_m}{RB_m + K_cK_uK_bK_sB_m + C_eC_l}.
\tag{12}
$$

Define the equivalent time constant by

$$
T_z = \frac{\left(R + K_cK_uK_bK_s\right)J_l}{N^2\left(RB_m + K_cK_uK_bK_sB_m + C_eC_l\right)}.
\tag{13}
$$

According to (11)–(13), (9) could be rewritten as

$$
\frac{\dot{\theta}_l}{i_{\text{ref}}} = \frac{C_lK_cK_u/N\left(RB_m + K_cK_uK_bK_sB_m + C_eC_l\right)}{T^2T_es^3 + T^2s^2 + \left(T_e + T_z\right)s + 1}.
\tag{14}
$$

Due to the small value of T_z, so

$$
T^2T_es^3 + T^2s^2 + \left(T_e + T_z\right)s + 1 \approx \left(T_es + 1\right)\left(T^2s^2 + 2\xi Ts + 1\right).
\tag{15}
$$

Then (14) could be further described by

$$
\frac{\dot{\theta}_l}{i_{\text{ref}}} = \frac{C_lK_cK_u/N\left(RB_m + K_cK_uK_bK_sB_m + C_eC_l\right)}{\left(T_es + 1\right)\left(T^2s^2 + 2\xi Ts + 1\right)},
\tag{16}
$$

where ξ is damp ratio.

Table 1 shows the system physical parameters. According to the experimental results, the current-loop parameters are $K_c = 0.8$, $K_b = 0.1$.

According to (9) and the parameters in Table 1, the generalized controlled object is

$$
G_p(s) = \frac{\dot{\theta}_l}{i_{\text{ref}}} = \frac{1.41 \times 10^4}{s^3 + 72.4s^2 + 7.58 \times 10^5 s + 5.47 \times 10^7}.
\tag{17}
$$

Equation (17) is discredited by adding zero-order hold, with sampling time $T = 0.001$ s,

$$
\begin{aligned}
G_p\left(z^{-1}\right) &= \frac{y_p(k)}{u(k)} = \frac{z^{-1}B_p\left(z^{-1}\right)}{A_p\left(z^{-1}\right)} \\
&= \frac{z^{-1}2.22 \times 10^{-6}\left(1 + 3.78z^{-1} + 0.965z^{-2}\right)}{1 - 2.219z^{-1} + 2.199z^{-2} - 0.9302z^{-3}}.
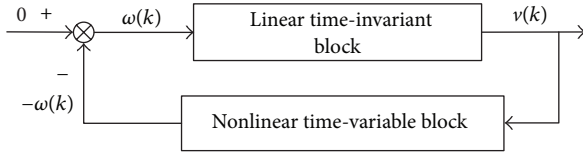\end{aligned}
\tag{18}
$$

FIGURE 7: Nonlinear feedback control system.

FIGURE 8: Structure of discrete MRAC system.

3.2. Reference Model.

According to (16), the system reference model is

$$G_m(s) = \frac{1}{(T_m s + 1)\left((s^2/\omega_m^2) + (2\xi s/\omega_m) + 1\right)}. \quad (19)$$

The reference model contains a first-order inertial system $F_1(s)$ and a second-order oscillation system $F_2(s)$:

$$F_1(s) = \frac{1}{T_m s + 1},$$

$$F_2(s) = \frac{1}{(s^2/\omega_m^2) + (2\xi s/\omega_m) + 1}. \quad (20)$$

According to the dynamic performance requirement and the structure characteristics of controlled object, the parameters of (19) are determined: $\omega_m = \omega_n = 869$, $\xi = 0.707$, and $T_m = 0.004$.

The reference model is described as

$$G_m(s) = \frac{1.89 \times 10^8}{s^3 + 1.48 \times 10^3 s^2 + 1.06 \times 10^6 s + 1.89 \times 10^8}. \quad (21)$$

Equation (21) is discredited by adding zero-order hold, with sampling time $T = 0.001$ s,

$$G_m(z^{-1}) = \frac{y_m(k)}{r(k)} = \frac{z^{-1}\beta_m B_m(z^{-1})}{A_m(z^{-1})}$$

$$= \frac{z^{-1} 0.0215\left(1 + 2.726 z^{-1} + 0.4756 z^{-2}\right)}{1 - 1.664 z^{-1} + 0.9818 z^{-2} - 0.2276 z^{-3}}. \quad (22)$$

4. Adaptive Controller Design Based on POPOV Super Stable Theory

4.1. POPOV Super Stable Theory.

As shown in Figure 7, a nonlinear feedback control system consists of a forward block and a nonlinear time-variable block. The linear time-invariant block is

$$x(k+1) = Ax(k) + B\omega(k),$$

$$v(k) = Cx(k) + D\omega(k). \quad (23)$$

The nonlinear time-variable block is

$$-\omega(k) = f(v(k), j, k), \quad k > j. \quad (24)$$

Define the discrete POPOV integral inequality by

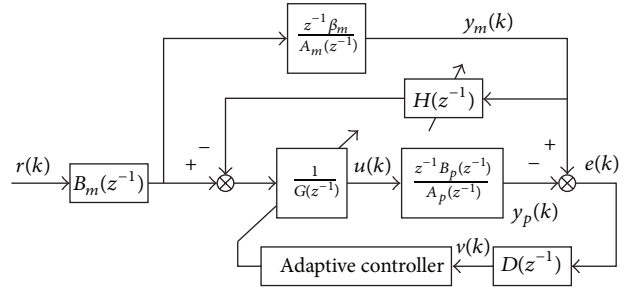$$-\sum_{k=0}^{k_1} \omega^T(k) v(k) \geq -r_0^2. \quad (25)$$

Discrete POPOV super stable theory is described as follows. If the control system, shown in Figure 7, meets the following conditions (a) and (b), the control system is globally asymptotic stable.

(a) The linear time-invariant block is strictly positive definite.

(b) The nonlinear time-variable block satisfies the discrete POPOV integral inequality (25).

4.2. Adaptive Control Law Design.

Figure 8 presents the structure of discrete MRAC system used in this paper. According to (18) and (22), the difference equation of controlled object can be described as

$$A_p(z^{-1}) y_p(k) = z^{-1} B_p(z^{-1}) u_p(k). \quad (26)$$

The difference equation of reference model can be described as

$$A_m(z^{-1}) y_m(k) = z^{-1} \beta_m B_m(z^{-1}) r(k). \quad (27)$$

$A_n(z^{-1})$, $B_n(z^{-1})$, $A_m(z^{-1})$, and $B_m(z^{-1})$ in (26) and (27) can be described as

$$A_p(z^{-1}) = 1 + \sum_{i=1}^{3} \hat{a}_i z^{-i}, \qquad B_p(z^{-1}) = \sum_{i=0}^{2} \hat{b}_i z^{-i},$$

$$A_m(z^{-1}) = 1 + \sum_{i=1}^{3} a_i z^{-i}, \qquad B_m(z^{-1}) = 1 + \sum_{i=1}^{2} b_i z^{-i}. \quad (28)$$

The values of $\hat{a}_i$, $\hat{b}_i$, a_i, and b_i are defined in (18) and (22).

From Figure 8, the following equation can be obtained:

$$B_m(z^{-1}) r(k) = H(z^{-1}) y_m(k) + G(z^{-1}) u_p(k), \quad (29)$$

where $H(z^{-1})$ and $G(z^{-1})$ are, respectively, feedback and feedforward multinomial,

$$H(z^{-1}) = \sum_{i=1}^{3} h_i(k) z^{-i+1}, \qquad G(z^{-1}) = \sum_{i=0}^{2} g_i(k) z^{-i}. \quad (30)$$

$D(z^{-1})$ is linear-compensator multinomial

$$D(z^{-1}) = 1 + \sum_{i=1}^{3} d_i z^{-i}. \quad (31)$$

Error $e(k)$ is defined as

$$e(k) = y_m(k) - y_p(k). \tag{32}$$

Substituting (29) into (27) and then subtracting (26), error equation is given as

$$e(k) = \frac{1}{A_p(z^{-1})} \omega(k), \tag{33}$$

where

$$\omega(k) = \sum_{i=1}^{3} [\widehat{a}_i - a_i + \beta_m h_i(k)] y_m(k-i)$$
$$+ \sum_{i=0}^{2} [\beta_m g_i(k) - \widehat{b}_i] u_p(k-i-1). \tag{34}$$

Considering the linear-compensator multinomial $D(z^{-1})$, the generalized error equation is

$$v(k) = D(z^{-1}) e(k) = \frac{D(z^{-1})}{A_p(z^{-1})} \omega(k). \tag{35}$$

As shown in Figure 7, $D(z^{-1})/A_p(z^{-1})$ is the linear time-invariant block and $-\omega(k)$ is the nonlinear time-variable block.

According to (18), the linear time-invariant block can be rewritten as

$$\frac{D(z^{-1})}{A_p(z^{-1})} = \frac{D(z^{-1})}{1 - 2.219z^{-1} + 2.199z^{-2} - 0.9302z^{-3}}. \tag{36}$$

According to the POPOV super stable theory, the linear time-invariant block (36) should be strictly positive definite. So the coefficients of $D(z^{-1})$ can be determined by

$$1 - d_1 + d_2 - d_3 > 0, \quad d_2 > -1, \ d_3 < 0.9. \tag{37}$$

When $h_i(k)$ and $g_i(k)$ are chosen as (38), the nonlinear time-variable block $-\omega(k)$ will satisfy the discrete POPOV integral inequality (25), which is proved at the end of this section:

$$h_i(k) = h_i(k-1) - \alpha_i v(k) y_m(k-i),$$
$$g_i(k) = g_i(k-1) - \beta_i v(k) u_p(k-i-1), \tag{38}$$

where $v(k) = e(k-1) + \sum_{i=1}^{3} d_i e(k-i-1); \alpha_i > 0, i = 1, 2, 3; \beta_i > 0, i = 0, 1, 2$.

As shown in Figure 8, the controller output $u(k)$ can be described as

$$u(k) = [r(k) B_m(z^{-1}) - H(z^{-1}) y_m(k)] \frac{1}{G(z^{-1})}$$
$$= [r(k) + b_1 r(k-1) + b_2 r(k-2) - h_1(k) y_m(k)$$
$$- h_2(k) y_m(k-1) - h_3(k) y_m(k-2)$$
$$- g_1(k) u(k-1) - g_2(k) u(k-2)] \frac{1}{g_0(k)}. \tag{39}$$

Now the proof of (38) meeting the discrete POPOV integral inequality is presented as follows.

The nonlinear time-variable block $-\omega(k)$ is given as

$$-\omega(k) = -\sum_{i=1}^{3} [\widehat{a}_i - a_i + \beta_m h_i(k)] y_m(k-i)$$
$$- \sum_{i=0}^{2} [\beta_m g_i(k) - \widehat{b}_i] u_p(k-i-1). \tag{40}$$

Equation (38) can be rewritten as

$$h_i(k) = h_i(-1) - \sum_{l=0}^{k} \alpha_i v(l) y_m(l-i),$$
$$g_i(k) = g_i(-1) - \sum_{l=0}^{k} \beta_i v(l) u_p(l-i-1). \tag{41}$$

Substituting (41) into (40), $-\omega(k)$ is rewritten as

$$-\omega(k)$$
$$= \sum_{i=1}^{3} \left[\beta_m \sum_{l=0}^{k} \alpha_i v(l) y_m(l-i) + a_i - \widehat{a}_i - \beta_m h_i(-1) \right]$$
$$\times y_m(k-i)$$
$$+ \sum_{i=0}^{2} \left\{ \beta_m \sum_{l=0}^{k} \beta_i v(l) u_p(l-i-1) + \widehat{b}_i - \beta_m g_i(-1) \right\}$$
$$\times u_p(k-i-1). \tag{42}$$

Substituting (42) into (25), the POPOV integral inequality is given as

$$-\sum_{k=0}^{k_1} \omega^T(k) v(k)$$
$$= \sum_{i=1}^{3} \left\{ \sum_{k=0}^{k_1} v(k) y_m(k-i) \right.$$
$$\times \left[\beta_m \sum_{l=0}^{k} \alpha_i v(l) y_m(l-i) + a_i - \widehat{a}_i - \beta_m h_i(-1) \right] \right\}$$
$$+ \sum_{i=0}^{2} \left\{ \sum_{k=0}^{k_1} v(k) u_p(k-i-1) \right.$$
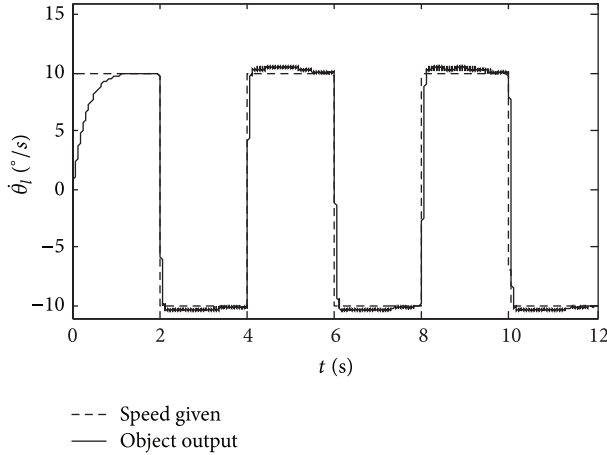$$\times \left[\beta_m \sum_{l=0}^{k} \beta_i v(l) u_p(l-i-1) + \widehat{b}_i - \beta_m g_i(-1) \right] \right\}. \tag{43}$$

FIGURE 9: System response with square-wave speed given.

In order to analyze (43), the following equation is introduced:

$$\sum_{k=0}^{k_1} x(k) \left\{ \sum_{l=0}^{k} [a x(l)] + c \right\}$$

$$= \frac{a}{2} \left[\sum_{k=0}^{k_1} x(k) + \frac{c}{a} \right]^2 + \frac{a}{2} \sum_{k=0}^{k_1} x^2(k) - \frac{c^2}{2a} \geq -\frac{c^2}{2a}, \quad (44)$$

$$a > 0.$$

According to (44), (43) meets the flowing inequality

$$-\sum_{k=0}^{k_1} \omega^T(k) \nu(k) \geq -\sum_{i=1}^{3} \beta_m \frac{\left[a_i - \widehat{a}_i - \beta_m h_i(-1)\right]^2}{2\alpha_i}$$

$$-\sum_{i=0}^{2} \beta_m \frac{\left[\widehat{b}_i - \beta_m g_i(-1)\right]^2}{2\beta_i}. \quad (45)$$

Due to $\beta_m > 0, \alpha_i > 0$, and $\beta_i > 0$, (45) can be further described as

$$-\sum_{k=0}^{k_1} \omega^T(k) \nu(k) \geq -r_0^2. \quad (46)$$

Equation (46) is the POPOV integral inequality. So (38) meeting the discrete POPOV integral inequality is proved.

5. Simulation Analyses

Simulation analyses are completed in Simulink of MATLAB 7.5. According to Figure 8, the simulation model is built. In the model, the adaptive controller is designed based on (22), (38)-(39), and the generalized controlled object is built based on Figure 5. The simulation parameters for adaptive controller are $d_1 = 1$, $d_2 = 1$, $d_3 = -1$, $\alpha_1 = \alpha_2 = \alpha_3 = 100$, and $\beta_1 = \beta_2 = \beta_3 = 1 \times 10^{-4}$.

When the speed given to the system is square-wave, the output speed wave is shown in Figure 9, and the waves of the

adaptive control parameters h_i and g_i are shown in Figure 10. As shown in Figures 9 and 10, after the second period, the controlled object output could keep up with reference model output, and the parameters h_i and g_i could also converge. The simulation results indicate that the adaptive control law proposed in this paper is feasible and effective.

6. Experimental Results

The DGCMG test system is originally developed by the Beijing University of Aeronautics and Astronautics in China. The experimental system is presented in Figure 11, and the schematic diagram is shown in Figure 12. The control system consists of power drive unit and signal processing unit. The proposed control algorithm is implemented in DSP TMS320C31 with a current-loop period of 200 μs and a speed-loop period of 1 ms. The control system receives speed given from the monitor computer through CAN bus. In order to observe the experimental results, the speed signals are displayed on the oscilloscope. The resolution of photoelectric encoder is $1.24''$.

According to the simulation results in Section 5, the parameters for adaptive controller are $K_c = 0.8$, $K_b = 0.1$, $d_1 = 1$, $d_2 = 1$, $d_3 = -1$, $\alpha_1 = \alpha_2 = \alpha_3 = 100$, and $\beta_1 = \beta_2 = \beta_3 = 1 \times 10^{-4}$.

In order to compare with MRAC, a PID controller is also adopted. As shown in Figure 5, the controllers of current and speed loops are all PID controllers. The current-loop parameters are $K_c = 0.8$ and $K_b = 0.1$. The proportional and integral coefficients for speed loop are $P = 20$, $I = 3500$. The speed feedforward coefficient is $K_f = 20$. The bandwidth and continuous-step tests are carried out to compare the performance of adaptive controller with that of PID controller.

6.1. Bandwidth Test. The speed given is $\dot{\theta}_{ref} = A \sin(2\pi f t)$, where $A = 10°$/s. When the speed frequency f is changed from 1 Hz to 3 Hz, the sine responses with PID controller and MRAC are shown in Figures 13 and 14.

When the speed frequency is 1 Hz, the tracking effect of PID controller is the same as that of MRAC. But when the speed frequency increases to 3 Hz, the tracking results of MRAC are obviously better than that of PID controller which has large overshoot and phase lag. And as shown in Figure 14, when speed frequency changes from 1 Hz to 3 Hz suddenly, the adaptive controller could make the object-output track the new frequency quickly. According to the experimental results, the system bandwidth is 2 Hz with PID controller and 3 Hz with MRAC.

6.2. Continuous Step-Response Test. Because the control period of real attitude control system is far less than that of the gimbal servosystem, the speed given to the gimbal is not continuous. So the continuous step-response test is carried out to verify the performance of gimbal system. The speed is continuously given by $0.1°$/s, $0.5°$/s, $2°$/s, $5°$/s, $8°$/s, and $10°$/s, with the time interval of 500 ms. The experimental results are shown in Figures 15 and 16.
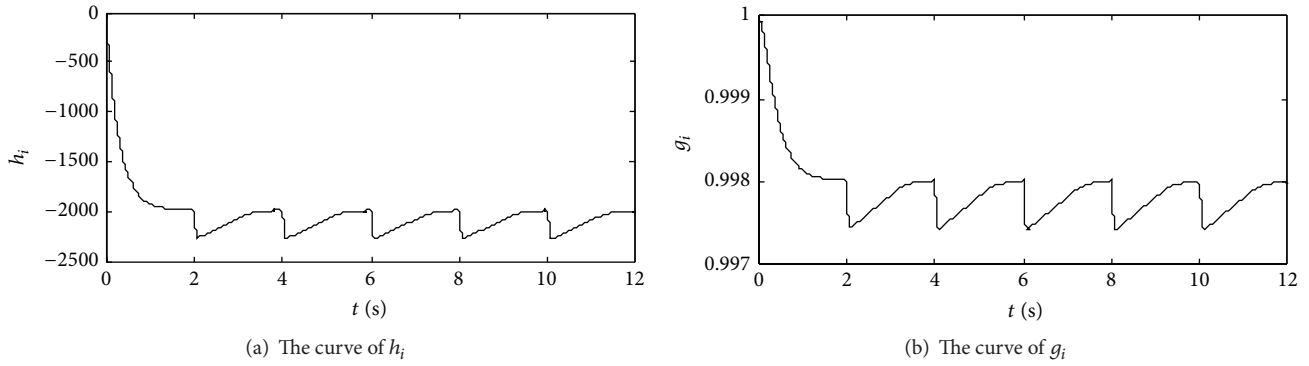
(a) The curve of h_i

(b) The curve of g_i

FIGURE 10: The curve of adaptive control parameters.
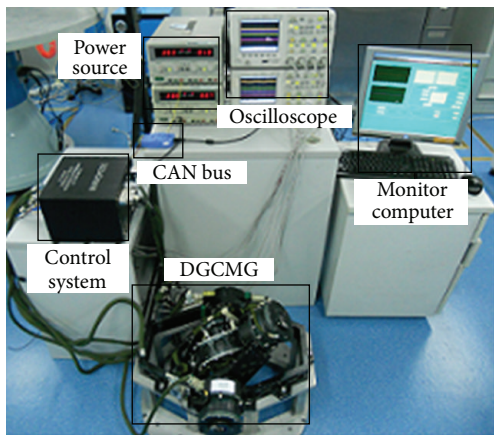
FIGURE 11: View of DGCMG test system.
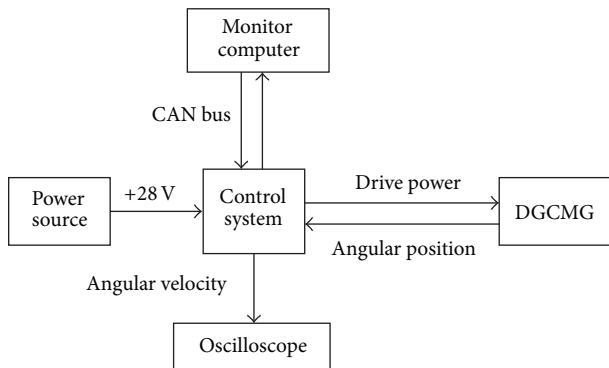
FIGURE 12: Schematic diagram of DGCMG test system.

--- Speed given
—— Object output

FIGURE 13: Sine response with PID controller, when the speed frequency is changed from 1 Hz to 3 Hz.

--- Speed given
—— Object output
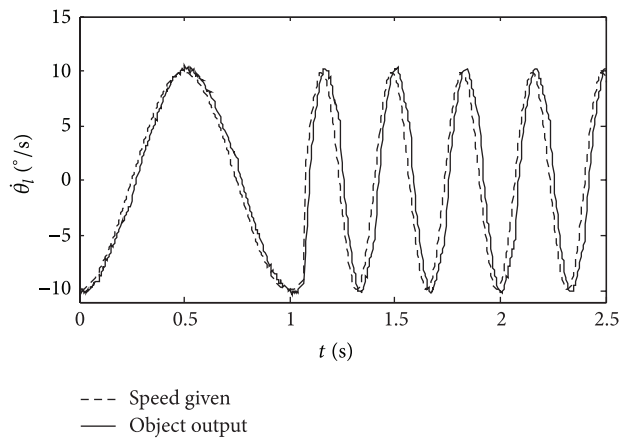
FIGURE 14: Sine response with MARC, when the speed frequency is changed from 1 Hz to 3 Hz.

As shown in Figure 15, PID controller has poor dynamic performances with obvious noises and large overshoot which can reach to 40%. And Figure 16 shows that adaptive controller has small overshoot and smooth response.

The experimental results of continuous step-response show that MRAC could improve the dynamic performance with small overshoot and make the system work smoothly without obvious noises.
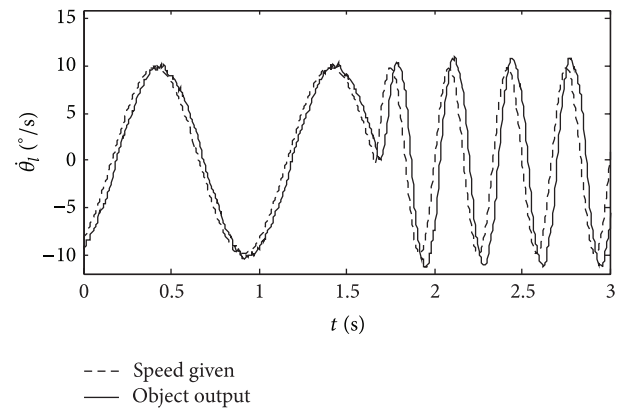
7. Conclusion

The DGCMG gimbal servosystem directly decides the performance of gyro moment. In order to improve the poor dynamic performance of gimbal servosystem caused by the low and nonlinear torsional stiffness of harmonic drive, a model reference adaptive control strategy is introduced in
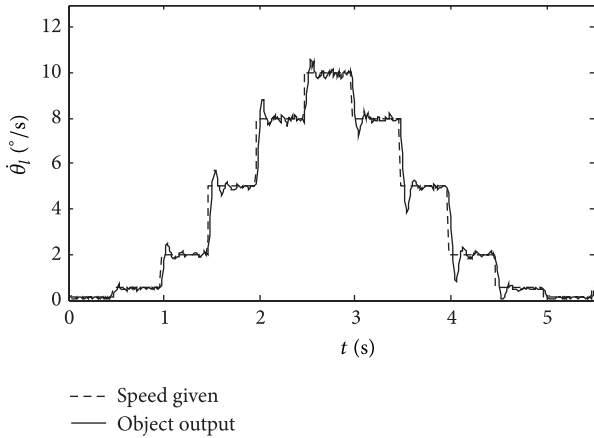
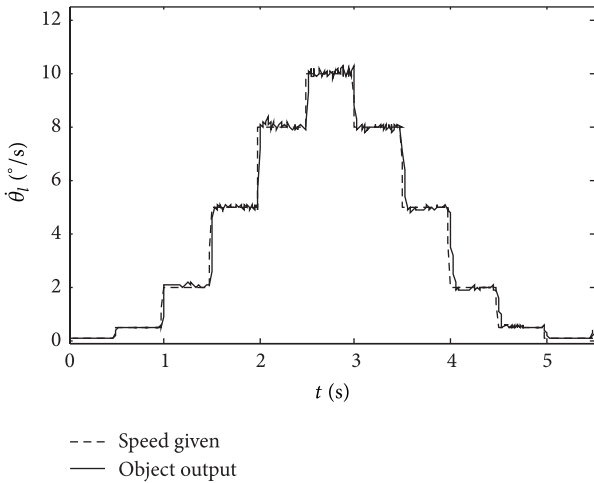FIGURE 15: Continuous step-response with PID controller.

FIGURE 16: Continuous step-response with MRAC.

this paper. Because only the input, output, and error are used and the measurement of the torque is not required, the proposed method is simple. In order to keep the fast dynamic response of current loop, the current loop and controlled object are treated as the generalized controlled object. The reference model is selected according the dynamic performance with fast response and small overshoot. The discrete POPOV super stable theory is used to design the adaptive controller. The model of DGCMG gimbal servosystem with harmonic drive is established. The MATLAB simulation results are provided to verify the effectiveness of the proposed control algorithm. The experimental results indicate that the MRAC could increase the bandwidth of gimbal servosystem to 3 Hz and improve the dynamic performance with small overshoot. And this method also has good engineering value.

Symbols

R: Stator winding resistance of torque motor
L: Stator winding inductance of torque motor
U: Stator voltage of torque motor
C_e: Back electromotive force (BEMF) coefficient of torque motor
C_l: Torque coefficient of torque motor
J_m: Rotational inertia of motor terminal including flexspline and toque motor rotor
J_l: Rotational inertia of load terminal including high-speed rotor and gyro-room
B_m: Damping coefficient of motor terminal including harmonic drive friction damping
B_l: Damping coefficient of load terminal
ϑ_m: Angle position of motor terminal
ϑ_l: Angle position of load terminal
ϑ: Torsion angle of harmonic drive
i_{ref}: Reference input of current loop
i_m: Stator current of torque motor
T_m: Output torque of torque motor
T_l: Output torque of harmonic drive
T_f: External disturbing torque including coupling gyro moment
K_e: Torsional stiffness of harmonic drive
N: Reduction ratio of harmonic drive
K_s: Amplification coefficient of current sampling circuit
K_u: Amplification coefficient of power driver circuit
K_f: Feedforward coefficient of speed loop
K_c: Proportionality coefficient of current loop
K_b: Feedback coefficient of current loop.

Acknowledgments

References

[1] S. P. Bhat and P. K. Tiwari, "Controllability of spacecraft attitude using control moment gyroscopes," *IEEE Transactions on Automatic Control*, vol. 54, no. 3, pp. 585–590, 2009.

[2] D. J. Krebs, "Model correlation of International Space Station Control Moment Gyroscope," in *Proceedings of the 39th AIAA/ASME/ASCE/AHS/ASC Structures, Structural Dynamics, and Materials Conference and Exhibit and AIAA/ASME/AHS Adaptive Structures Forum*, pp. 813–818, April 1998, AIAA-98-1793.

[3] J. Ahmed, "Adaptive control of double-gimbal control moment gyro with unbalanced rotor," *Journal of Guidance, Control, and Dynamics*, vol. 25, no. 1, pp. 105–115, 2002.

[4] C. J. Heiberg, "A practical approach to modeling singal-gimbal control momentum gyroscope in agile spacecraft," in *Proceedings of AIAA Guidance, Navigation, and Control Conference and Exhibit*, pp. 1–11, 2000, AIAA-2000-4545.

[5] J. C. Fang and Y. Ren, "High-precision control for a single-gimbal magnetically suspended control moment gyro based on inverse system method," *IEEE Transactions on Industrial Electronics*, vol. 58, no. 9, pp. 4331–4341, 2001.

[6] J. Fang, S. Zheng, and B. Han, "AMB vibration control for structural resonance of double-gimbal control moment gyro with high-speed magnetically suspended rotor," *IEEE/ASME Transactions on Mechatronics*, vol. 18, no. 1, pp. 32–43, 2013.

[7] T. D. Tuttle and W. P. Seering, "A nonlinear model of a harmonic drive gear transmission," *IEEE Transactions on Robotics and Automation*, vol. 12, no. 3, pp. 368–374, 1996.

[8] F. H. Ghorbel, P. S. Gandhi, and F. Alpeter, "On the kinematic error in harmonic drive gears," *Journal of Mechanical Design*, vol. 123, no. 1, pp. 90–97, 2001.

[9] P. S. Gandhi and F. H. Ghorbel, "Closed-loop compensation of kinematic error in harmonic drives for precision control applications," *IEEE Transactions on Control Systems Technology*, vol. 10, no. 6, pp. 759–768, 2002.

[10] R. Dhaouadi, F. H. Ghorbel, and P. S. Gandhi, "A new dynamic model of hysteresis in harmonic drives," *IEEE Transactions on Industrial Electronics*, vol. 50, no. 6, pp. 1165–1171, 2003.

[11] G. Zhang and J. Furusho, "Speed control of two-inertia system by PI/PID control," *IEEE Transactions on Industrial Electronics*, vol. 47, no. 3, pp. 603–609, 2000.

[12] K. Szabat and T. Orlowska-Kowalska, "Vibration suppression in a two-mass drive system using PI speed controller and additional feedbacks—comparative study," *IEEE Transactions on Industrial Electronics*, vol. 54, no. 2, pp. 1193–1206, 2007.

[13] S. E. Saarakkala, M. Hinkkanen, and K. Zenger, "Speed control of two-mass mechanical loads in electric drives," in *Proceedings of the IEEE Energy Conversion Congress and Exposition (ECCE '12)*, pp. 1246–1253, 2012.

[14] H. Chaoui and P. Sicard, "Adaptive neural network control of flexible-joint robotic manipulators with friction and disturbance," in *Proceedings of the 38th Annual Conference on IEEE Industrial Electronics Society (IECON '12)*, pp. 2644–22649, 2012.

[15] W. H. Zhu, E. Dupuis, M. Doyon, and J. C. Piedboeuf, "Adaptive control of harmonic drives based on virtual decomposition," *IEEE/ASME Transactions on Mechatronics*, vol. 11, no. 5, pp. 604–614, 2006.

[16] L. Tian and A. A. Goldenberg, "Robust adaptive control of flexible joint robots with joint torque feedback," in *Proceedings of the IEEE International Conference on Robotics and Automation*, pp. 1229–1234, May 1995.

[17] I. Hassanzadeh, H. Kharrati, and J. R. Bonab, "Model following adaptive control for a robot with flexible joints," in *Proceedings of the IEEE Canadian Conference on Electrical and Computer Engineering (CCECE '08)*, pp. 1467–1472, May 2008.

[18] Z. M. Doina, "LQG/LQR optimal control for flexible joint manipulator," in *Proceedings of the International Conference and Exposition on Electrical and Power Engineering (EPE '12)*, pp. 35–40, October 2012.

[19] C. Trautman and D. Wang, "Experimental H_∞ control of a single flexible link with a shoulder joint," in *Proceedings of the IEEE International Conference on Robotics and Automation*, vol. 1, pp. 1235–1241, May 1995.

[20] K. H. Kim, "Model reference adaptive control-based adaptive current control scheme of a PM synchronous motor with an improved servo performance," *IET Electric Power Applications*, vol. 3, no. 1, pp. 8–18, 2009.

[21] S. Zhang and Y. Pi, "Model reference adaptive control application study in PM synchronous motor servo system," in *Proceedings of the 2nd Conference on Power Electronics and Intelligent Transportation System (PEITS '09)*, pp. 428–432, December 2009.

[22] L. Yacoubi, K. Al-Haddad, L. A. Dessaint, and F. Fnaiech, "A DSP-based implementation of a nonlinear model reference adaptive control for a three-phase three-level NPC boost rectifier prototype," *IEEE Transactions on Power Electronics*, vol. 20, no. 5, pp. 1084–1092, 2005.

[23] K. Y. Huang, H. C. Chin, and Y. C. Huang, "A model reference adaptive control strategy for interruptible load management," *IEEE Transactions on Power Systems*, vol. 19, no. 1, pp. 683–689, 2004.

[24] D. H. Lee and J. W. Ahn, "A current ripple reduction of a high-speed miniature brushless direct current motor using instantaneous voltage control," *IET Electric Power Applications*, vol. 3, no. 2, pp. 85–92, 2009.